Ocean Modelling 39 (2011) 332–350

Contents lists available at ScienceDirect

Ocean Modelling

journal homepage: www.elsevier.com/locate/ocemod

Sensitivity analysis of three-dimensional salinity simulations in North San Francisco Bay using the unstructured-grid SUNTANS model

Vivien P. Chua *, Oliver B. Fringer

Environmental Fluid Mechanics Laboratory, Dept. of Civil and Environmental Engineering, Stanford University, Stanford, CA 94305, United States

ARTICLE INFO

Article history:
Received 18 February 2011
Received in revised form 11 May 2011
Accepted 23 May 2011
Available online 6 June 2011

Keywords:
Unstructured grid
Numerical diffusion
Scalar advection scheme
Turbulence model
Grid resolution

ABSTRACT

The unstructured-grid SUNTANS model is applied to San Francisco Bay using a grid with an average resolution of 50 m. This accurately resolves tidal hydrodynamics in a domain that extends from the Pacific Ocean to the western portion of the Delta region, the flow through which is approximated with two rectangular boxes as a "false delta". A detailed calibration is performed, and we show that the model accurately predicts tidal heights, currents, and salinity at several locations throughout the Bay. We perform a sensitivity study to understand the effects of grid resolution, the turbulence model, and the scalar transport scheme. Three levels of grid refinement are performed, and the results of a second-order accurate, TVD scalar transport scheme are compared to those with first-order upwinding. We find that the best convergence rate with respect to grid refinement occurs when the TVD scheme is employed. This accuracy degrades when the turbulence model is not employed due to a lack of feedback between vertical turbulent mixing and stratification. Significant horizontal diffusion associated with first-order upwinding eliminates the necessary horizontal salinity gradients required to induce baroclinic circulation, and renders the results less sensitive to the turbulence model or grid refinement.

1. Introduction

San Francisco Bay consists of two distinct subestuaries: the northern reach lies between the Golden Gate and the confluence of the Sacramento–San Joaquin Rivers and comprises San Pablo Bay, Suisun Bay and Central Bay, and South Bay extends southward from the Golden Gate to San Jose (Fig. 1). The northern reach is a partially-mixed estuary dominated by seasonally varying freshwater inflows, while South Bay is a tidally oscillating lagoon-type estuary. Spatial and temporal variability in San Francisco Bay are characterized by tides, freshwater inflow, and exchange with coastal waters (Walters et al., 1985; Conomos et al., 1985; Conomos, 1979). Tides in San Francisco Bay are mixed semi-diurnal and diurnal with pronounced spring-neap variability. San Francisco Bay receives most of its freshwater inflow from the Sacramento–San Joaquin Delta. During periods of low inflow, seawater penetrates upstream to the confluence of the Sacramento and San Joaquin rivers, while high inflows result in enhanced salinity stratification and gravitational circulation, with a salt wedge developing around Carquinez Strait (Conomos, 1979; Kimmerer, 2002). Seasonal variability in nearshore oceanic circulation in the Pacific results in seasonal variability in the composition of the coastal waters that enter San Francisco Bay (Largier, 1996), and this has important implications for seasonal phytoplankton dynamics (Cloern and Nichols, 1985).

Two- and three-dimensional models have been applied extensively to numerical simulations of circulation in San Francisco Bay. Cheng et al. (1993) developed a two-dimensional depth-averaged model of San Francisco Bay with TRIM2D (Casulli, 1990) which is calibrated and validated with a large set of surface elevation and current data. The two-dimensional TRIM model has been implemented in the San Francisco Bay Marine Nowcast System (Cheng and Smith, 1998), and realtime Nowcast model results are available for download. The TRIM3D model (Casulli and Cattani, 1994) (three-dimensional version of TRIM2D) has been applied to San Francisco Bay to study hydrodynamics resulting from salinity-induced baroclinic circulation. A conservative transport method and a two-equation turbulence closure model are added to TRIM3D by Gross et al. (1999b), and the resulting model is used to investigate the effects of stratification in South Bay. Gross et al. (2010) recently presented the results of TRIM3D as applied to the entire San Francisco Bay, and details of the calibration are presented along with an assessment of model performance which performs extremely well throughout the Bay. The UnTRIM model (Casulli and Walters, 2000), which is the unstructured version of TRIM3D and is the methodology upon which the SUNTANS model (Fringer et al., 2006) is based, has also been applied to San Francisco Bay by MacWilliams and Cheng (2006).

Successful applications of two- and three-dimensional models to estuaries like San Francisco Bay depend heavily on accurate

* Corresponding author. Tel.: +1 650 450 1124.
E-mail address: vchua@stanford.edu (V.P. Chua).

1463-5003/$ - see front matter © 2011 Elsevier Ltd. All rights reserved.
doi:10.1016/j.ocemod.2011.05.007

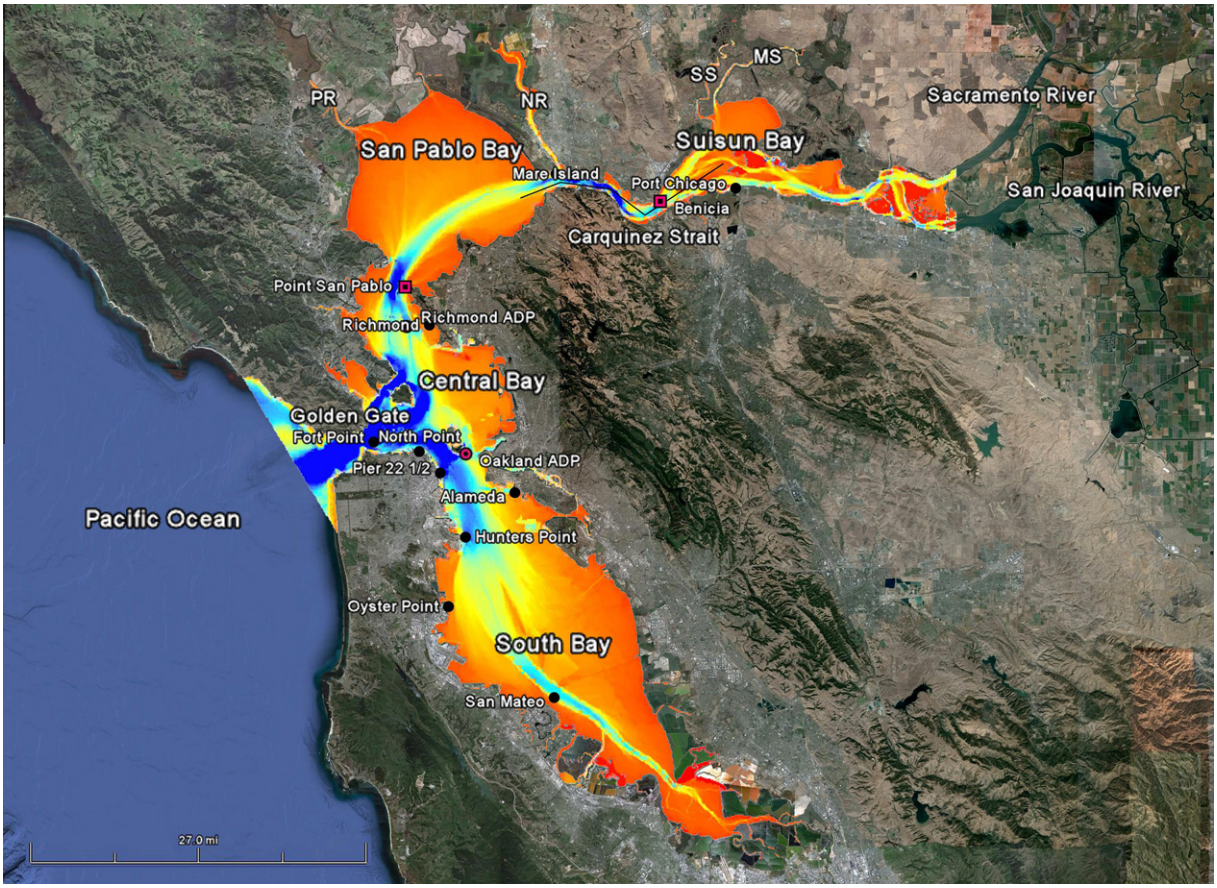

Fig. 1. The San Francisco Bay model domain, bathymetry (in m) and locations of calibration. Legend: Surface elevations (black circles), currents (red circles), salinity (red squares), and vertical profile transect (black line), Petaluma River (PR), Napa River (NP), Suisun Slough (SS), Montezuma Slough (MS). (For interpretation of the references to colour in this figure legend, the reader is referred to the web version of this article.)

implementation of the advection scheme, which requires consistency with continuity (Gross et al., 2002), accurate specification of boundary conditions (i.e., inflows, ocean salinity, and precipitation/evaporation), and an accurate scalar transport algorithm. Specification of the turbulence model also influences model results, where popular choices are two-equation models such as $k-kl$ (Mellor–Yamada 2.5), $k-\epsilon$ and $k-\omega$ schemes. Hence, understanding effects of the scalar advection scheme relative to the turbulence model is crucial to accurately simulate flows in periodically stratified estuaries.

In this paper, we describe the setup and implementation of the SUNTANS model as applied to San Francisco Bay. Details of the calibration are presented, and model performance is assessed via validation against observations of sea-surface heights, currents, and salinity at several locations throughout the Bay. A TVD scalar transport scheme is implemented and the results are compared to those using first-order upwinding. A sensitivity study is performed to determine the effects of grid resolution, the turbulence model, and the scalar transport scheme on salinity simulations in North San Francisco Bay.

2. Governing equations and numerical method

We employ the SUNTANS model (Fringer et al., 2006) to simulate the flow in San Francisco Bay. SUNTANS is a parallel nonhydrostatic coastal ocean solver that uses a finite-volume formulation to solve the hydrodynamics and scalar transport equations. Although SUNTANS is a nonhydrostatic model, the present implementation is hydrostatic since the dynamics of interest are strongly hydrostatic. The governing equations are the three-dimensional, Reynolds-averaged primitive equations:

$$\frac{\partial u}{\partial t}+\nabla\cdot(\mathbf{u}u)-fv=-g\frac{\partial h}{\partial x}-g\frac{\partial r}{\partial x}+\nabla_H\cdot(\nu_H\nabla_H u)+\frac{\partial}{\partial z}\left(\nu_V\frac{\partial u}{\partial z}\right), \tag{1}$$

$$\frac{\partial v}{\partial t}+\nabla\cdot(\mathbf{u}v)+fu=-g\frac{\partial h}{\partial y}-g\frac{\partial r}{\partial y}+\nabla_H\cdot(\nu_H\nabla_H v)+\frac{\partial}{\partial z}\left(\nu_V\frac{\partial v}{\partial z}\right), \tag{2}$$

where the free-surface height is h, the velocity vector is $\mathbf{u}$ and $u(x,y,z,t)$ and $v(x,y,z,t)$ are the Cartesian velocity components in the x and y directions, and the vertical velocity $w(x,y,z,t)$ in the vertical z direction is computed via continuity:

$$\nabla\cdot\mathbf{u}=0. \tag{3}$$

The baroclinic head is given by

$$r=\frac{1}{\rho_0}\int_z^h \rho dz, \tag{4}$$

where ρ_0 is the constant reference density and the total density is given by $\rho_0+\rho$. The Coriolis term is given by $f=2\Omega\sin\phi$, where ϕ is the latitude and Ω is the angular velocity of the earth. The horizontal and vertical eddy-viscosities are given by ν_H and ν_V,

respectively. The free-surface evolves according to the depth-averaged continuity equation:

$$\frac{\partial h}{\partial t}+\frac{\partial}{\partial x}\left(\int_{-d}^{h} u dz\right)+\frac{\partial}{\partial y}\left(\int_{-d}^{h} v dz\right)=0. \tag{5}$$

The density perturbation, ρ, is computed with a linear equation of state in terms of the salinity s using $\rho=\rho_0(1+\beta(s-s_0))$, where ρ_0 and s_0 are reference states and $\beta=7.5\times10^{-4}$ psu^{-1} is the coefficient of salt expansivity. The effects of temperature on the stratification are neglected. The transport equation for salinity neglects horizontal diffusion and is given by

$$\frac{\partial s}{\partial t}+\nabla\cdot(\mathbf{u}s)=\frac{\partial}{\partial z}\left(\gamma_V\frac{\partial s}{\partial z}\right), \tag{6}$$

where γ_V is the vertical turbulent eddy-diffusivity. These equations are solved using the methods described in Fringer et al. (2006), in which the free-surface height, vertical diffusion of momentum, and vertical scalar advection and diffusion are advanced implicity with the theta-method, and all other terms are advanced with the second-order Adams–Bashforth method. For advection of momentum, the Eulerian–Lagrangian method (ELM) is employed and is crucial for successful applications that incorporate wetting and drying (Wang et al., 2008).

2.1. Bottom shear stress and turbulence closure

The quadratic drag law is applied at the bottom boundary to compute the bottom stress with

$$\tau_b=\rho_0 C_d U_1\mathbf{u}_1, \tag{7}$$

where $\mathbf{u}_1$ is the horizontal velocity vector in the first grid cell above the bed and $U_1=\sqrt{\mathbf{u}_1\cdot\mathbf{u}_1}$ is its magnitude, and the drag coefficient C_d is computed from the bottom roughness parameter z_0 with:

$$C_d=\left[\frac{1}{\kappa}\ln\left(\frac{z_1}{z_0}\right)\right]^{-2}. \tag{8}$$

Here, z_1 is the location of U_1 at a distance of one-half the bottommost vertical grid spacing above the bed, and the roughness coefficient z_0 is adjusted to calibrate the three-dimensional model. The surface elevations are relatively insensitive to the choice of z_0, and z_0 is chosen so that the predicted velocities show a good level of agreement. No further tuning of z_0 is required for salinity calibrations. A spatially-varying z_0 is used, such that in the Bay, $z_0=0.001$ mm, and in shallow regions (with depths less than 1.0 m), $z_0=1$ mm. No interpolation of z_0 is done, as we found that smooth transition over depths did not significantly change our results. Areas of marshland in San Pablo Bay and Suisun Bay account for the larger values of $z_0=1$ mm, as intense vegetation in these shallow shoal regions can significantly increase the bottom drag (Nepf, 1999). Similar values of z_0 are used for the intertidal zone by Wang et al. (2008) and for depths less than 2.0 m in simulations of South Bay by Gross et al. (1999a). Estimates of z_0 by Cheng et al. (1999) show substantial variability of between 10 and 0.01 mm. Our choice of $z_0=0.001$ mm is smaller than values used by Gross et al. (1999a) in South Bay ($z_0=0.02$ mm) and from field experiments (Cheng et al., 1999). This small value is likely necessary to partially compensate for errors due to numerical diffusion when using ELM for advection of momentum (Wang et al., 2008).

The horizontal turbulent mixing of momentum in SUNTANS is determined with a constant eddy-viscosity, while it is ignored for advection of scalars. The Mellor–Yamada level 2.5 (MY2.5) model (Mellor and Yamada, 1982), with stability functions modified by Galperin et al. (1988) is used to compute the vertical eddy-viscosity and eddy-diffusivity. Details of the implementation of the turbulence model in SUNTANS are described in Wang et al. (2011). A comparison of turbulence closure schemes in the Snohomish River estuary shows that differences between the schemes are relatively minor (Wang et al., 2011).

2.2. Wet-dry treatment

The wet-dry treatment is developed in SUNTANS by Wang et al. (2008) and is used to simulate the flooding and draining of marshlands in the Bay. The buffering layer with thickness $h_{buffer}=0.1$ m is defined in which the drag coefficient is increased to $C_d=5$ in order to decelerate the flow when the water depth becomes very shallow. This is on the same order of magnitude as values used by Ip et al. (1998) ($h_{buffer}=0.25$ m), while Wang et al. (2008) and Zheng and Liu (2003) used $h_{buffer}=0.05$ m. Our choice of $C_d=5$ for dry cells follows from values used by Wang et al. (2008). For cells with water depth greater than h_{buffer}, the drag coefficient is computed from Eq. (8). A minimum depth h_{dry} is defined to ensure positive depth for numerical stability. Cells with depth less than h_{dry} are considered dry and tagged inactive. Wang et al. (2008) noted that the choice of h_{dry} is arbitrary, and we use $h_{dry}=0.05$ m.

2.3. Numerical method for scalar transport

A variety of scalar transport schemes for unstructured grids are available to interpolate scalar concentrations defined at cell centers of staggered grids to their cell faces (Darwish and Moukalled, 2003; Casulli and Zanolli, 2005). Typical implementations of higher-order monotonicity-preserving schemes interpolate face values using a combination of first-order upwinding and a higher-order antidiffusive flux, the value of which is limited using a flux-limiter to ensure monotonicity via the TVD (Total Variation Diminishing) constraint (Harten, 1983). If the flux limiter is zero, then the scheme reverts to first-order upwinding, while other values of the limiter, which depend solely on the ratio of the upwind to the local scalar concentration gradient, depend on the particular limiter function which is devised to yield different properties. For example, in second-order accurate, five-point TVD schemes for the one-dimensional advection equation, the Superbee limiter (Roe, 1984) is the largest possible value of the limiter that still retains monotonicity for one-dimensional advection, while the Minmod limiter (Sweby, 1984) is the smallest possible value that ensures TVD and second-order accuracy. The Superbee scheme typically compresses fronts (Fringer and Street, 2005; Gross et al., 1999a), while limiters that are closer to the Minmod scheme tend to smooth fronts. When applied to multidimensions on Cartesian grids, operator splitting is required if the TVD properties are to be ensured (Gross et al., 1999b), while on unstructured grids further limitations on the fluxes are required (Casulli and Zanolli, 2005).

We implemented the TVD formulation of Casulli and Zanolli (2005) in SUNTANS, which allows specification of any of the existing flux limiters. Rather than presenting a comparison of numerous advection schemes as was done by Gross et al. (1999a) for South Bay, our focus is on the quantitative differences between a low- and a high-order scheme, and therefore we restrict comparison to two schemes, namely one that uses first-order upwind and the second of which employs the Superbee limiter. In the presence of wetting and drying, if a face abuts a dry cell, then first-order upwinding is always employed. This has a negligible effect on the overall character of the advection. In this paper we refer to the scheme that employs the Superbee limiter as the TVD scheme, and this scheme is employed for the calibration simulations.

3. Setup of San Francisco Bay simulation

3.1. Computational domain

The computational domain depicted in Fig. 1 spans between the Pacific Ocean and the western and central portions of the Sacramento–San Joaquin Delta, including Central Bay, San Pablo Bay, Suisun Bay and South Bay. The ocean boundary extends to approximately 40 km west of Golden Gate. The radius of the semi-circular ocean boundary is chosen to align the northern most open boundary with Point Reyes. The complex and interconnected network of tributaries in the Sacramento-San Joaquin Delta is represented by a "false delta" consisting of two rectangles (Gross et al., 2005). This allows specification of inflow conditions emerging from the Delta. The length and depth of the "false deltas" are sized to obtain the correct tidal behavior of the Delta as seen by the eastern boundary of the SUNTANS domain.

The major watercourses included in the domain are the Petaluma and Napa rivers which drain into San Pablo Bay, and the Suisun and Montezuma slough which feed into Suisun Bay (see Fig. 1). The smaller rivers, creeks and tributaries entering San Francisco Bay do not provide significant inflows and are not included in the smiulations because they do not significantly affect the salinity results over the 1.5-month simulation period presented in this paper.

3.2. Bathymetry

The model uses bathymetric data obtained from the National Geophysical Data Center (NGDC) database. The bathymetry was derived from US National Ocean Service (NOS) soundings in San Francisco Bay and the coastal ocean. The bathymetric source uses raw depths that have not been gridded and the average resolution of the soundings in the Bay is 10 m. Based on the work by Gross et al. (2005), a constant depth of 20 m is assumed for the rectangular "false deltas". The vertical datum is defined as mean sea level (MSL). We find the resolution of the bathymetry is sufficient for this study as the bathymetric data set used to interpolate the depths to cell centers of the unstructured grid has higher resolution than the resolution of the grid. The bathymetry of San Francisco Bay is shown in Fig. 1.

3.3. Unstructured grid

The unstructured grid for the domain (Fig. 2) was generated using SMS (Environmental Modeling Systems, Inc.). The average resolution of the grid, based on triangular cell lengths, is 50 m, and the grid resolution gradually becomes larger west of the Golden Gate. The gradual transition in grid cell lengths prevents numerical errors associated with abrupt transitions in grid size. SUNTANS uses an orthogonal unstructured mesh, and a metric of orthogonality for San Francisco Bay is shown in Fig. 3. Angle skewness is the maximum deviation from 60° among the three angles of a cell. The average angle skewness for this grid is 8.5°.

In the vertical, the grid has structured z-levels, with a maximum of 60 layers in the deepest portion of the domain. The minimum vertical resolution is in the top layer and is 0.29 m. The vertical resolution is refined in the upper layers with a stretching ratio of 10% moving downward to resolve the flow in shallow regions of the Bay and in the vicinity of the salt wedge at Carquinez Strait. Partial

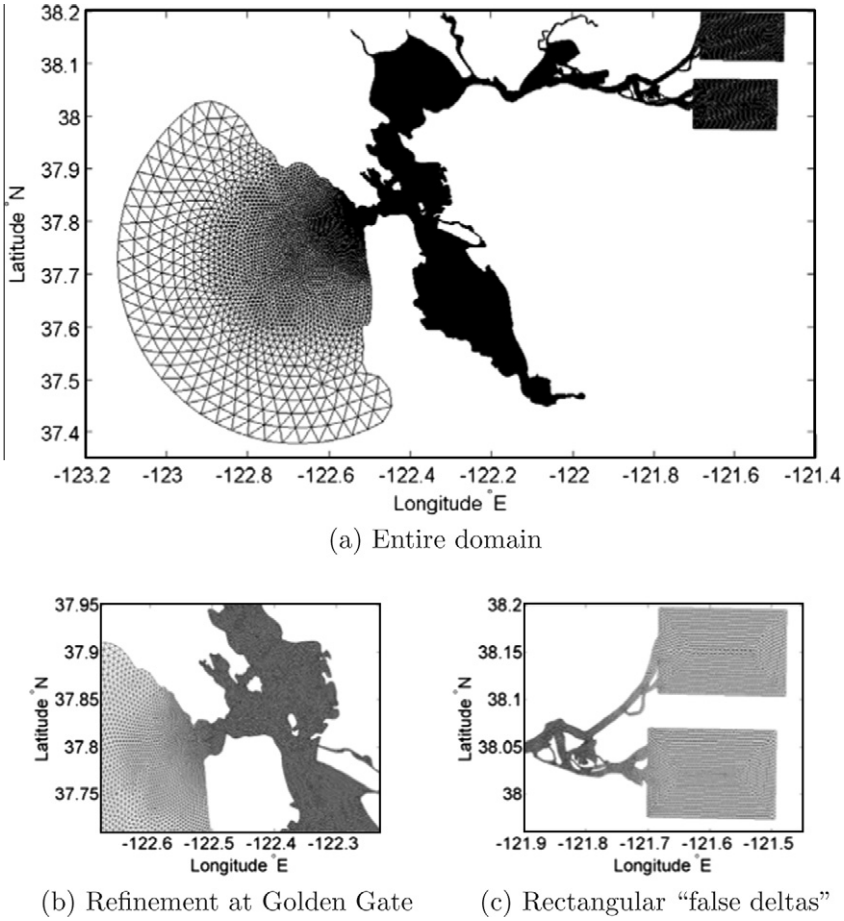

Fig. 2. The unstructured grid of San Francisco Bay. Entire domain (a), refinement at Golden Gate (b), and rectangular "false deltas"(c).

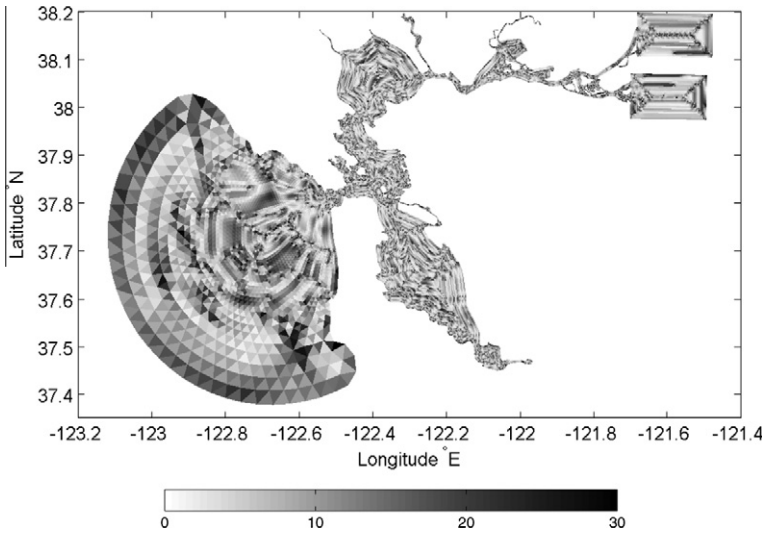

Fig. 3. Metric of orthogonality for San Francisco Bay. Greyscale depicts the distribution of angle skewness, in degrees.

stepping is employed so that the bottom faces of the bottom-most cells coincide with the interpolated depth at the cell centers. The total number of cells in the horizontal is approximately 80,000 with more than 80% located in the Bay. The three-dimensional grid has approximately 2.5 million grid cells.

3.4. Initial and boundary conditions

The simulation is initialized with a flat free surface and a quiescent velocity field. The ocean salinity is assumed to be 33.5 psu, which corresponds to typical values observed in the coastal ocean near San Francisco Bay (Dever and Lentz, 1994). The salinity field in the Bay was initialized with US Geological Survey (USGS) synoptic observations collected on 11 January, 2005. The dataset consists of vertical profiles of salinity at 1 m vertical resolution at 39 sampling locations along the longitudinal axis of San Francisco Bay. The salinity at the cell centers of the grid is obtained by interpolation using the three nearest-neighbors with an inverse-distance weighting scheme. Because salinity observations are available in the main channel along the central axis of the Bay but not in the shoals, the initial conditions assume no lateral variation in salinity. By initializing salinity with the observed data, the spin-up time is reduced from approximately 30 days if the domain is initialized with ocean salinity to 15 days.

Open boundaries are located at the Pacific Ocean and at the Sacramento–San Joaquin Delta. The model is tidally forced at all nodes along the Pacific Ocean boundary with the 8 major tidal constituents from observed water surface elevations at Point Reyes (a single point). Specification of amplification and phase lag is not required when using observations at Point Reyes to drive the open ocean boundary, unlike the tidal boundary condition employed by Gross et al. (2005).

The Sacramento–San Joaquin Delta boundary is forced with freshwater inflow estimates from the DAYFLOW program (CDWR, 1986). Daily-averaged flows at San Joaquin river past Jersey Point (QWEST) and Sacramento river past Rio Vista (QRIO) are used to force the open boundaries at the rectangular "false deltas". The DAYFLOW program estimates flow using a volume balance

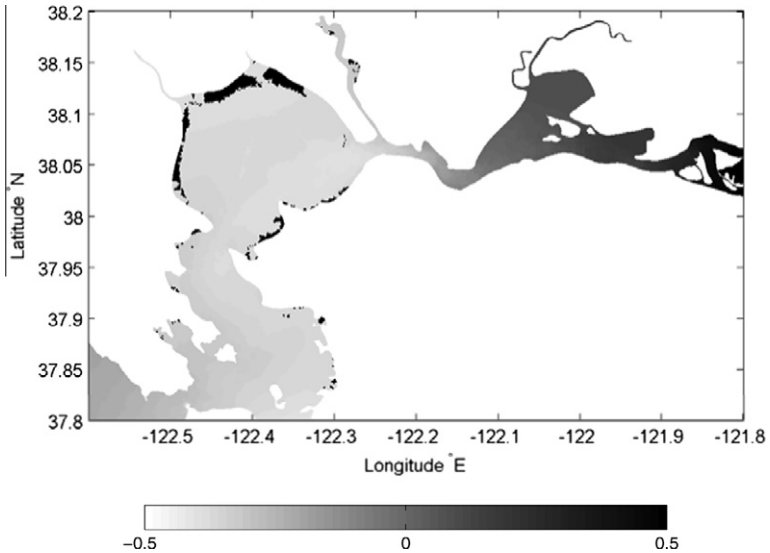

Fig. 4. Intertidal mudflats in North San Francisco Bay are exposed during LLW (shown in black). Surface elevations (in m) on the wet areas are plotted for day 30.9.

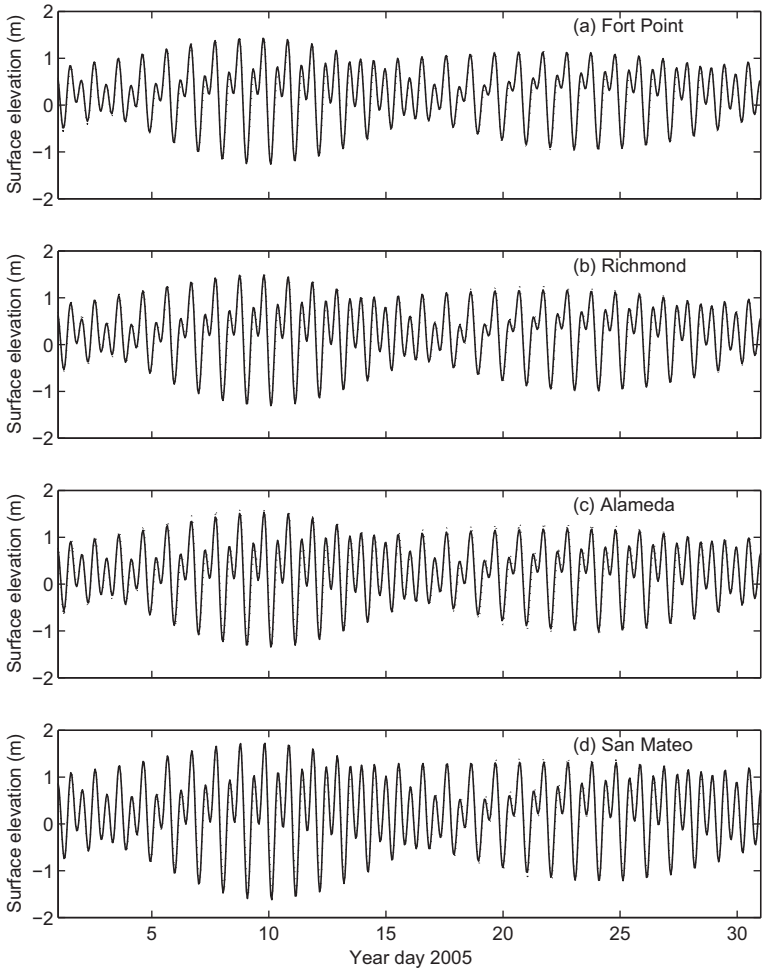

Fig. 5. Comparison of predicted and observed surface elevations (in m) at (a) Fort Point, (b) Richmond, (c) Alameda and (d) San Mateo Bridge. Legend: predictions (···), observations (—).

Table 1
Statistical evaluation of surface elevations.

Station	RMS error (m)	RMS error (%)	Correlation coefficient
Fort Point	0.088	3.3	0.99
Richmond	0.098	3.5	0.99
Alameda	0.13	4.6	0.98
San Mateo	0.11	3.3	0.99

approach, and can contain substantial errors due to uncertain terms in the water balance. Flow monitoring data collected by Oltmann (1998) suggest that the actual daily-averaged flows might be very different from DAYFLOW estimates. The cross-sectionally averaged velocities are imposed by dividing the inflow fluxes by the cross-sectional area at the Delta boundaries. The cross-sectionally averaged velocity is given by

Table 2
M2 surface elevation constituents.

Station	Amplitude (m)			Phase (°)		
	Observed	Predicted	Error	Observed	Predicted	Error
Central Bay						
Fort Point	0.580	0.586	−0.006	210.6	211.0	−0.4
Richmond	0.616	0.612	0.004	223.1	231.2	−8.1
South Bay						
North Point	0.607	0.624	−0.017	213.3	221.1	−7.8
Pier 22 1/2	0.644	0.658	−0.014	218.9	226.4	−7.5
Alameda	0.678	0.709	−0.031	224.0	229.5	−5.5
Hunters Point	0.706	0.720	−0.014	223.6	228.4	−4.8
Oyster Point	0.753	0.762	−0.009	235.5	230.0	5.5
San Mateo	0.826	0.814	0.012	238.0	231.9	6.1
North Bay						
Mare Island	0.597	0.659	−0.062	260.6	254.6	6.0
Port Chicago	0.515	0.424	0.091	288.2	277.5	10.7

$$u_b = \frac{Q_{\text{flow}}}{A_b}, \tag{9}$$

where A_b is the surface area of the boundary and Q_{flow} is the inflow flux estimated from the DAYFLOW program. A_b is computed for each time step as the surface area changes with the tides.

A 45-day simulation is run during the period 1 January 2005 – 14 February 2005. In the winter river inflow is relatively high, and hence the influence of coastal upwelling/downwelling is negligible in our model. The surface elevations, currents and salinity from the 45-day run are compared to observations for the period in which field data are available. A time step size of 10 s is employed and is dictated by stability of explicit horizontal advection of scalars, which requires, approximately:

$$\Delta t \leqslant \min\left(\frac{\Delta x_i}{|u_i|}\right), \tag{10}$$

the minimum of which occurs where the Voronoi distance between adjacent cells is $\Delta x_i = 20$ m and the velocity is $u_i = 2$ m s^{-1}, and this occurs at the Golden Gate. Using this time step, simulation of the 45-day period requires 388,800 time steps which consumes 108 h

Table 3
K1 surface elevation constituents.

Station	Amplitude (m)			Phase (°)		
	Observed	Predicted	Error	Observed	Predicted	Error
Central Bay						
Fort Point	0.368	0.378	−0.010	226.5	230.2	−3.7
Richmond	0.374	0.360	0.014	233.1	241.5	−8.4
South Bay						
North Point	0.376	0.377	−0.001	226.8	236.2	−9.4
Pier 22 1/2	0.381	0.381	0.000	229.5	239.0	−9.5
Alameda	0.377	0.377	0.000	232.7	241.8	−9.1
Hunters Point	0.394	0.385	0.009	232.1	240.8	−8.7
Oyster Point	0.400	0.388	0.012	238.3	242.0	−3.7
San Mateo	0.401	0.396	0.005	239.5	243.0	−3.5
North Bay						
Mare Island	0.336	0.336	0.000	253.7	255.2	−1.5
Port Chicago	0.287	0.196	0.091	271.9	278.8	−6.9

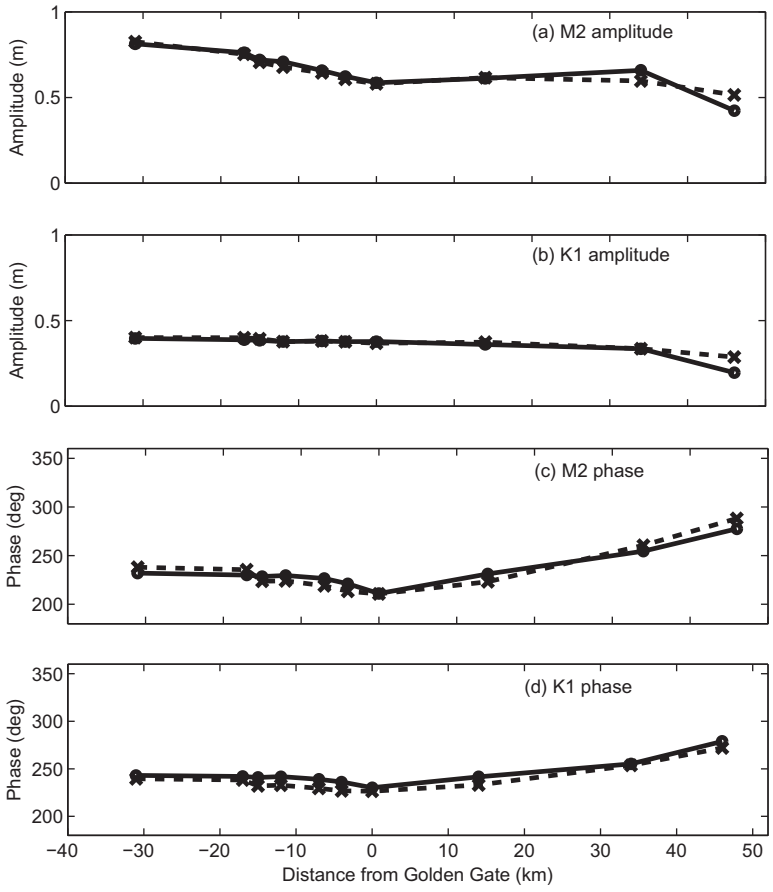

Fig. 6. Distribution of amplitudes (in m) and phases (in degrees) for M2 and K1 harmonics plotted against distance from Golden Gate. Distances in South Bay are negative and those in North Bay are positive. Legend: predictions (−o−), observations (−x−).

of wallclock time using 32 processors on the Peter A. McCuen Environmental Computing Center at Stanford University. One wallclock second is therefore required to compute 10 s of simulation time, and thus simulations run roughly ten times faster than real time.

The horizontal eddy-diffusivity is ignored, while the background vertical eddy-diffusivity is set to $\nu = 10^{-6}\ \mathrm{m^2\ s^{-1}}$ which is required to allow turbulence to grow due to production in the turbulence model. The Coriolis parameter is assumed constant and is given by $f = 9.36 \times 10^{-5}\ \mathrm{rad\ s^{-1}}$. We neglect winds in our simulations as they do not influence the predictions over the time scale of interest. Winds may be more important for longer time-scale predictions. The implementation of wet-dry treatment in SUNTANS allows for the flooding and draining of the intertidal zones. Fig. 4 depicts the exposed areas in North San Francisco Bay during a strong low tide around day 30.9, where areas along the boundary in San Pablo Bay become dry.

4. Model calibration and validation

4.1. Surface elevations

Surface elevation calibrations were performed via comparison to observations at NOAA stations throughout San Francisco Bay (Fig. 1). The predicted and observed surface elevations at four NOAA stations in the Bay, namely: (a) Fort Point (9414290), (b) Richmond (9414863), (c) Alameda (9414750), and (d) San Mateo Bridge (9414458) are shown in Fig. 5. The diurnal and semi-diurnal tidal ranges and spring-neap tidal cycle are well reproduced by the model at all stations. The predicted and observed surface elevations at Golden Gate show very good agreement, indicating that the ocean boundary condition is accurately specified. The surface elevations at Richmond, Alameda and San Mateo Bridge are also predicted reasonably well both in terms of tidal range and phase. Overall, the surface elevation calibrations demonstrate that the model is accurately propagating tides along the axis of the estuary.

Similar metrics to those of Gross et al. (2010), including mean and RMS errors and the correlation coefficients, are used for model skill assessment. We compute mean and RMS errors of time series with N elements using:

$$\text{Mean error} = \frac{1}{N}\sum (X_{\text{model}} - X_{\text{obs}}), \tag{11}$$

$$\text{RMS error} = \frac{1}{N}\sqrt{\sum (X_{\text{model}} - X_{\text{obs}})^2}, \tag{12}$$

where X is the desired quantity to compare, i.e. free-surface, depth-averaged currents, or salinity. The correlation coefficient is computed with:

$$r = \frac{\sum \left(X_{\text{model}} - \overline{X}_{\text{model}}\right)\left(X_{\text{obs}} - \overline{X}_{\text{obs}}\right)}{\sqrt{\left(\sum \left(X_{\text{model}} - \overline{X}_{\text{model}}\right)\right)\left(\sum_i \left(X_{\text{obs}} - \overline{X}_{\text{obs}}\right)\right)}} \tag{13}$$

where $\overline{X}$ is the quantity averaged over the calibration period. Statistical evaluation of the model performance for surface elevations is presented in Table 1. At the NOAA stations, the RMS errors are less than 5% of the tidal range and correlation coefficients exceed 0.98.

Harmonic analysis of surface elevations is carried out at NOAA stations where harmonic constituent data are available. A comparison of observed and predicted amplitudes and phases for the M2 constituent is shown in Table 2. The amplitude and phase errors are within 9 cm and 11°, respectively for all stations. The observed and predicted K1 harmonics are shown in Table 3. The errors for amplitudes and phases are within 9 cm and 10°, respectively. The effect of errors of S1, O1 and N2 harmonics on the tidal hydrodynamics are negligible as their amplitudes on the order of 0.1, 0.2 and 0.1 m, respectively, are relatively small when compared to the M2 and K1 harmonics which are on the order of 0.6 m and 0.3 m, respectively, and so the S1, O1 and N2 data are not shown. The spatial distributions of the amplitude and phases for the M2 and K1 harmonics are plotted in Fig. 6, which shows that the errors in the predicted M2 and K1 amplitudes increase with distance from the Golden Gate. This occurs because of bathymetric variability upstream that makes accurate specification of bottom roughness a difficult task, particularly where the shallow mudflats are extensive.

Table 4
Statistical evaluation of depth-averaged velocities (in m s^{-1}).

Station	Observed mean	Predicted mean	Mean error	RMS error
Richmond				
U	−0.0093	−0.0022	0.0071	0.11
V	0.057	−0.0044	0.061	0.16
Oakland				
U	−0.030	−0.0040	0.026	0.065
V	−0.074	0.017	0.096	0.17

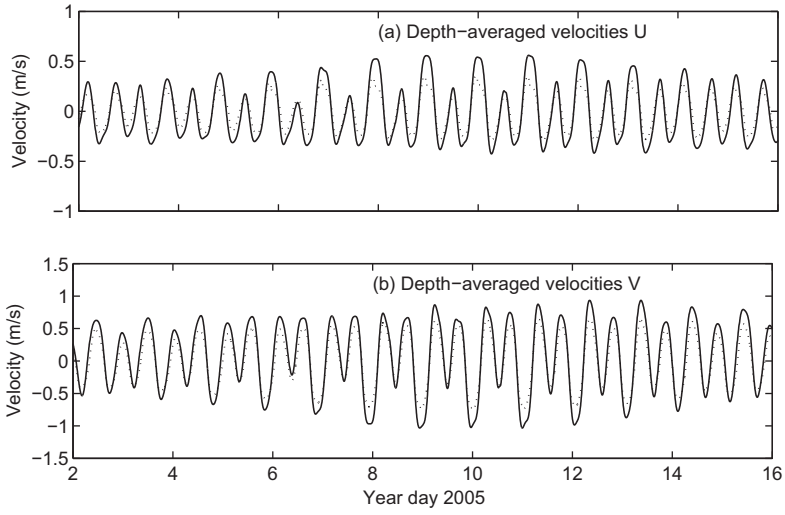

Fig. 7. Comparison of predicted and observed depth-averaged velocities (in m s^{-1}) at Richmond. Legend: predictions (···), observations (—).

4.2. Currents

Acoustic doppler profiler (ADP) current data are obtained from NOAA/NOS at two stations in San Francisco Bay, namely (a) Richmond and (b) Oakland. Current data is available at the ADP stations from 1 January 2005 (year day 1) – 30 January 2005 (year day 30). The locations of the ADP stations are shown in Fig. 1. The raw ADP current data is filtered with a low-pass fifth-order Butterworth filter, with the cutoff frequency of seven cycles/day to remove the high-frequency non-tidal oscillations, following the approach of Sankaranarayanan and McCay (2003). The phase shift inherent to the Butterworth filter is eliminated by passing the current data forward and backward through the filter. The U and V directions are chosen as the east and north components of the velocities, respectively. A statistical evaluation of the model performance for the depth-averaged U and V velocities is presented in Table 4. The mean and RMS errors are computed with Eqs. (11) and (12) where X is either the depth-averaged U or V velocity.

As shown in Figs. 7 and 8, the model reproduces the spring-neap variability and the mixed diurnal and semi-diurnal variability in the observed currents at Richmond. The depth-averaged velocities in Fig. 7 show the phases of the U and V velocities compare well, and overall a good level of agreement is obtained for the magnitudes. Peak U and V depth-averaged velocities are slightly underpredicted by the model. U and V velocity profiles in Fig. 8 compare well throughout the water column. U velocity profiles close to the bottom are slightly underpredicted during flood and ebb. We attribute these errors to two sources. First, the Richmond ADP is located close to the intertidal mudflats and hence the flow at Richmond is influenced by wetting and drying of the mudflats, which is subject to numerical errors as a result of strong gradients inherent in the observations that may not be resolved by the

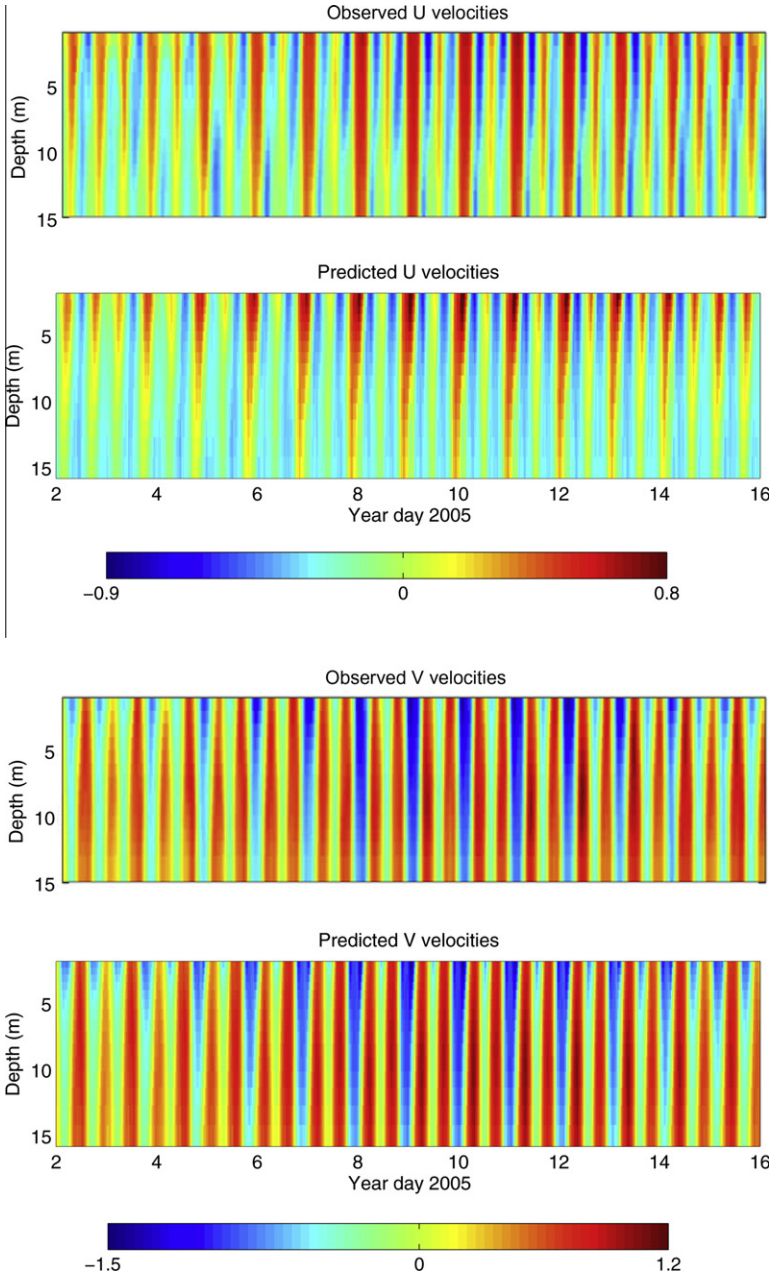

Fig. 8. Comparison of predicted and observed U and V velocity profiles (in m s^{-1}) at Richmond.

simulations. Second, the accuracy of predicting velocities in the bottom half of the water column is dependent on accurate representation of the bottom shear layer which is difficult to capture correctly in the presence of strong bathymetric variability.

As shown in Figs. 9 and 10, at Oakland the model-predicted currents have similar spring-neap cycles and mixed diurnal and semi-diurnal patterns as the observed velocities. The phases and magnitudes of the U and V depth-averaged velocities show good overall agreement. The depth-averaged velocities in Fig. 9 show that the peak ebb U velocities are underpredicted by the model during spring tides, while peak flood U velocities are overpredicted by the model during neap tides. During spring tides peak flood V velocities are overpredicted by the model, and peak ebb V velocities are underpredicted by the model. V velocity profiles in Fig. 10 compare well throughout the water column, while U velocity profiles close to the surface during ebb are underpredicted by our model and U velocity profiles close to the bottom during flood are overpredicted by our model. The difficulty in obtaining good predictions at Oakland is due to the complex flow around Treasure Island and Yerba Buena Island which is highly variable, and may not be well-resolved by the resolution in our model.

4.3. Salinity

The salinity calibration is performed from 15 January 2005 (year day 15) to 15 February 2005 (year day 45). We calibrated salinity for this period as it takes at least 15 days to spin-up the three-dimensional salinity simulations. The salinity predictions are compared with observations from the US Geological Survey (USGS) at two locations in San Francisco Bay, namely: (a) Point San Pablo (PSP) and (b) Benicia (BEN) (shown in Fig. 1). The salinity observations consist of both near-surface and near-bottom salinity at both stations. The observed salinity data is filtered with a low-pass fifth-order ButterWorth filter to remove non-tidal oscillations, and forward and backward passed to eliminate the phase shift inherent in the filter.

Time series of surface and bottom salinity, and bottom-top salinity difference at Point San Pablo are shown in Fig. 11. In general, there is good qualitative agreement between the predicted and observed salinities in terms of amplitude and phase. The predicted stratification compares well with observations, with the exception that our model predicts lower maximum stratification (3 psu) from year day 48 to year day 50, as a consequence of overprediction of minimum surface salinity during this period.

Time series of surface and bottom salinity, and bottom-top salinity difference at Benicia are shown in Fig. 12. The salinity predictions are generally in good agreement with the observations. The predicted onset and breakdown of stratification occurs roughly with the correct magnitude and phase relative to the observations. Periodically stratified conditions are present during spring tides, in which the water column is well-mixed during the strong tide and weakly stratified during the weak tide. The minimum stratification from our model is relatively insensitive to the spring-neap variability. The errors may be due to inaccuracies in the inflow estimates from DAYFLOW, the effects of which are larger when the strength of the tidal currents is weak. Flow boundary conditions imposed at the Delta use daily-averaged flow values, and this averaging may also contribute to the errors.

Statistical evaluation of the model performance for salinity is presented in Table 5. The mean and RMS errors are computed with Eqs. (11) and (12), respectively. The mean errors at PSP at the surface and bottom sensors are 0.14 and 0.25 psu, respectively, while the RMS errors at the surface and bottom sensors are 1.4 and 1.2 psu, respectively. Our mean errors are lower than that of Gross et al. (2010), in which the mean errors for the surface and bottom sensors are 1.0 and 0.8 psu, respectively (Gross et al. (2010) did not compute RMS errors for salinity). MacWilliams et al. (2007) compared bottom salinities at this station, and found mean and RMS errors of 1.22 and 1.70 psu, respectively.

The mean errors at Benicia at the surface and bottom sensors are 0.08 and 0.36 psu respectively, while the RMS errors at the surface and bottom sensors are 1.2 and 1.4 psu, respectively. At a nearby location (Martinez in Carquinez Straits) Gross et al. (2010) found mean errors for the surface and bottom sensors of 0.5 and 1.4 psu, respectively. MacWilliams et al. (2007) computed the mean and RMS errors at the bottom sensors to be 1.56 and 2.21 psu, respectively. Overall, our model therefore has errors that are lower than the three-dimensional simulations of San Francisco Bay performed with TRIM (Gross et al., 2010) and UnTRIM (MacWilliams et al., 2007). We will show that our model produces lower errors due to differences in grid resolution.

5. Model sensitivity

5.1. Sensitivity to grid resolution

To understand model sensitivity with respect to grid resolution, we perform simulations with three different levels of horizontal

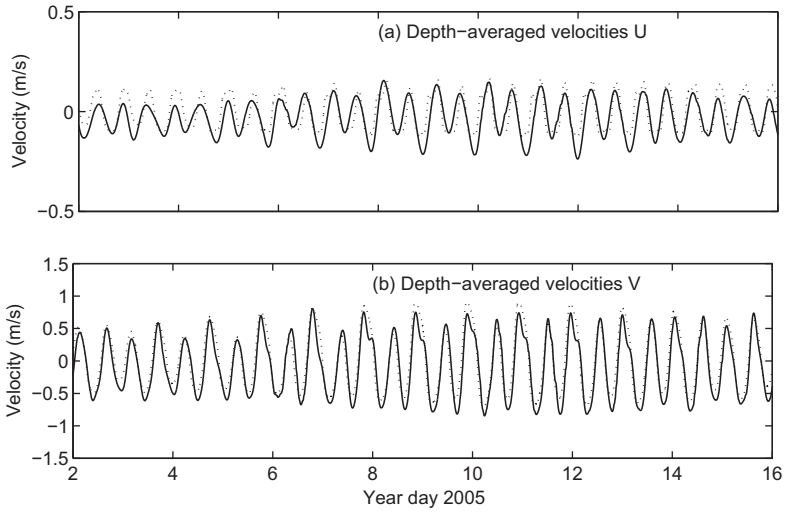

Fig. 9. Comparison of predicted and observed depth-averaged velocities (in m s^{-1}) at Oakland. Legend: predictions (···), observations (—).

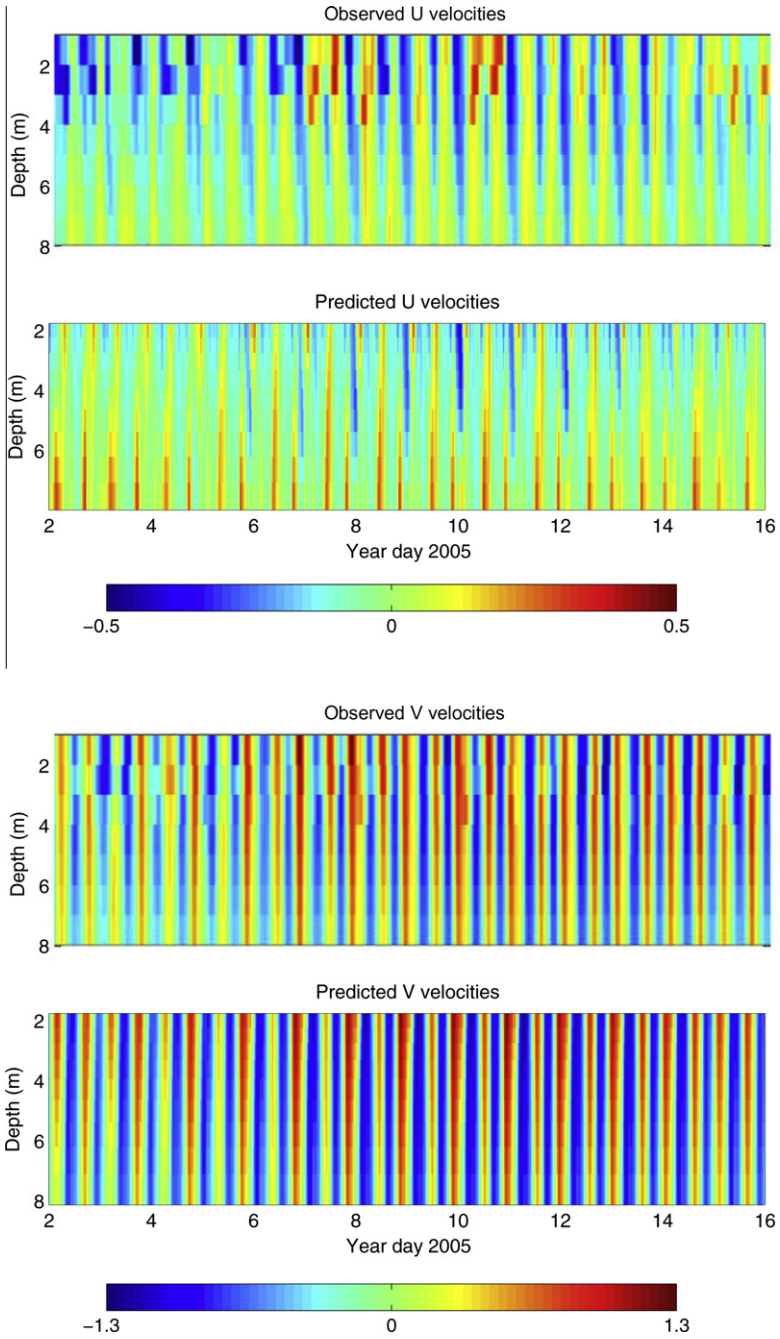

Fig. 10. Comparison of predicted and observed U and V velocity profiles (in m s^{-1}) at Oakland.

grid refinement. The coarse mesh has grid cell edge lengths of 200 m in the Bay, the medium mesh has grid cell edge lengths of 100 m in the Bay and the fine mesh has grid cell edge lengths of 50 m in the Bay. The fine mesh results correspond to those presented in the previous calibration section. For all three meshes, the grid resolution gradually becomes larger west of the Golden Gate. The vertical structured *z*-level grid is not changed. Comparisons of salinity predictions with observations are made at Benicia and Point San Pablo with the three levels of grid resolution. We perform the simulations on each mesh with four different scenarios to evaluate the relative effects of the scalar transport scheme and the turbulence model. The scenarios are referred to as: (A) TVD with turbulence model, (B) TVD without turbulence model, (C) First-order upwind with turbulence model, (D) First-order upwind without turbulence model. When the turbulence model is not employed, this implies that we ignore vertical eddy-diffusivity in the scalar transport equation by setting it to zero, although vertical eddy-viscosity is still retained in the momentum equations. All other parameters are the same as those presented in the previous calibration section.

The mean and RMS errors in the bottom salinity at Benicia and Point San Pablo are plotted as a function of grid refinement in Fig. 13. The most obvious source of error in the plots is the monotonic increase in errors moving from scenario *A* to *D* for a fixed grid resolution (*A* possessing the smallest error and *D* possessing the largest error). The largest increase in error occurs from implementation of first-order upwind for scalar advection, which is apparent in both the mean and RMS errors. The second greatest source of

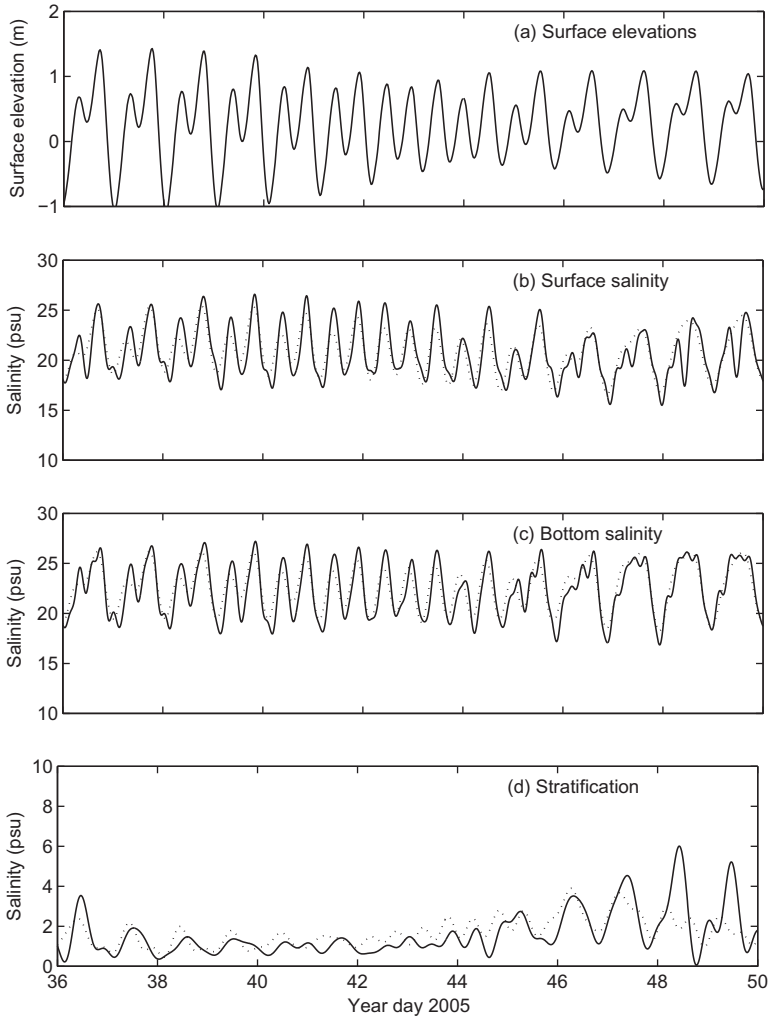

Fig. 11. Comparison of predicted and observed salinities (in psu) at Point San Pablo: (a) surface elevations, (b) surface salinity, (c) bottom salinity, (d) stratification. Surface and bottom salinities are 7.9 m and 0.9 m from the bottom, respectively. Legend: predictions (···), observations (—).

error results from implementation of the turbulence model. Lack of the turbulence model, and hence lack of vertical eddy-diffusivity, leads to a greater error for all levels of grid refinement. The impact of the turbulence model is relatively weak for all cases except for its impact on the mean salinity error when the TVD scheme is employed (runs *A* and *B*). Although the impact of not using the turbulence model on the mean salinity is large for these cases, the mean error in the bottom salinity is the same without the turbulence model on the fine mesh as that with the turbulence model on the coarse mesh.

Fig. 13 shows that convergence with respect to grid refinement is achieved with the TVD advection scheme (runs *A* and *B*), but convergence is extremely weak for the first-order scheme (runs *C* and *D*). This is shown with the least squares fitted convergence rates tabulated in Table 6. For runs *A* and *B*, convergence is near 1.5-order with respect to grid refinement for the mean error. However, convergence is weaker for the RMS error. Although second-order convergence is expected for the one-dimensional five-point TVD schemes (Roe, 1984), errors arising from implementation on the unstructured grid reduce the rate of convergence to less than second order.

The depth-averaged salinity at a particular location within the salt wedge can be approximated by assuming that it lies in a region of relatively constant horizontal salinity gradient Γ (Monismith et al., 2002), such that:

$$s(t) = S - \frac{u\Gamma}{\omega}\sin(\omega t), \tag{14}$$

where S is the time- and depth-averaged salinity, and u is the magnitude of the depth-averaged tidal currents at frequency ω. If we denote an observed value with subscript o and a modeled or predicted value with subscript p, then the error in the salinity can be approximated by

$$\Delta s(t) = s_p(t) - s_o(t) = \Delta S - \frac{u\Delta\Gamma}{\omega}\sin(\omega t),$$

where $\Delta S = S_p - S_o$ and $\Delta\Gamma = \Gamma_p - \Gamma_o$, and we have assumed that most of the error arises from differences in the modeled salinity field and not in the depth-averaged currents u. Denoting the time-average over a period $2\pi/\omega$ with an overbar gives the time-average of the error as:

$$\overline{\Delta s(t)} = \Delta S,$$

and the RMS error as:

$$\left(\overline{(\Delta s - \overline{\Delta s})^2}\right)^{1/2} = \left(\overline{\Delta s^2} - \left(\overline{\Delta s}\right)^2\right)^{1/2} = \frac{1}{\sqrt{2}}\frac{u\Delta\Gamma}{\omega}.$$

This shows that the mean error indicates errors in the time- and depth-averaged salinity at a point, while the RMS error depends more strongly on errors in the horizontal salinity gradient, i.e.

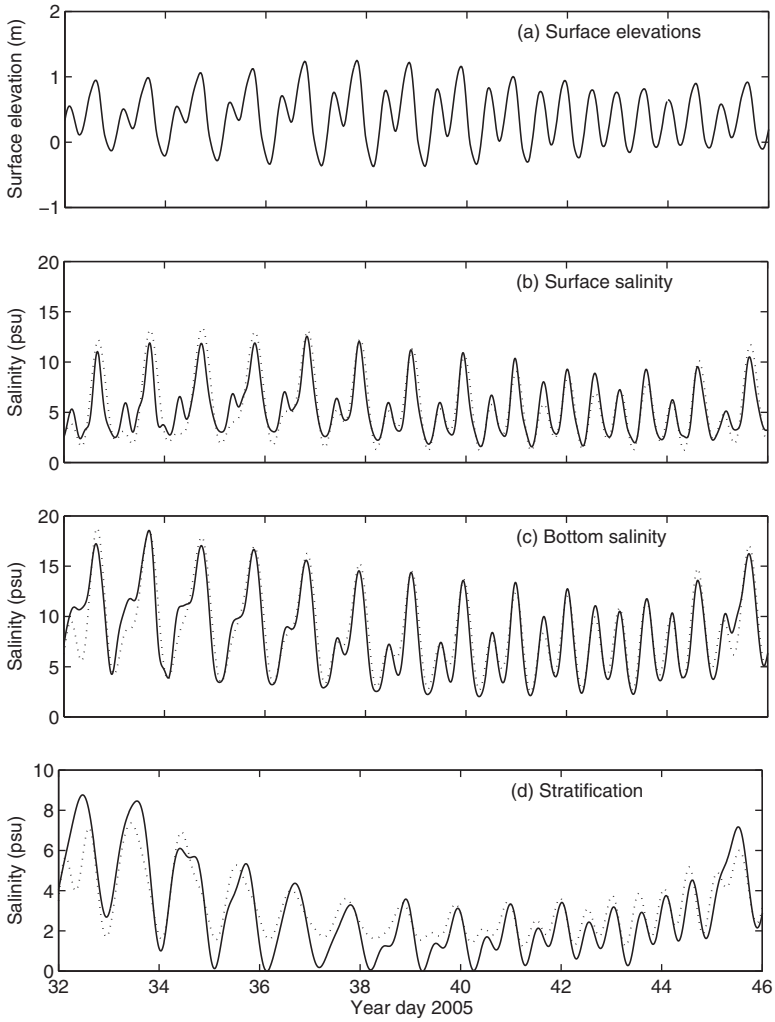

Fig. 12. Comparison of predicted and observed salinities (in psu) at Benicia: (a) surface elevations, (b) surface salinity, (c) bottom salinity, (d) stratification. Surface and bottom salinities are 22.5 m and 7.6 m from the bottom, respectively. Legend: predictions (···), observations (—).

Table 5
Statistical evaluation of salinity (in psu).

Station	Observed mean	Predicted mean	Mean error	RMS error
Point San Pablo (PSP)				
Surface	20.7	20.9	0.14	1.4
Bottom	22.3	22.6	0.25	1.2
Benicia Bridge (BEN)				
Surface	5.3	5.4	0.08	1.2
Bottom	8.2	8.6	0.36	1.4

$\Delta\Gamma$. Hence, the mean error is a measure of model ability to produce the correct salinity intrusion, and the RMS error is a measure of model ability to reproduce horizontal salinity gradients. This implies that model ability to predict salinity values converges at near 1.5-order, while model ability to predict salinity gradients converges with less than first order. Since both Benicia and Point San Pablo lie within the salt wedge, the errors at the two locations behave similarly. However, convergence rates at Point San Pablo are slightly higher (see Table 6), and this may be due to smoother bathymetry and weaker currents there.

Despite an expected first-order convergence rate, Fig. 13 shows that use of the first-order upwinding scheme (runs *C* and *D*) exhibits its lack of convergence for the grid resolutions employed. The relative impact of the turbulence model on the errors is also negligible when first-order upwinding is employed. We hypothesize that lack of convergence occurs because excessive numerical diffusion due to first-order upwinding eliminates the feedback mechanism between vertical turbulent mixing and stratification. This is exhibited by the ineffectiveness of the turbulence model in reducing the errors for first-order upwinding in Fig. 13. On the other hand, when the TVD scheme is employed, the nonlinear feedback causes a reduction in errors by roughly one order of magnitude (the difference between run *A* and run *B*).

As shown in Fig. 14, the impact of first-order upwinding is not only to reduce the horizontal salinity gradient, but also to reduce the vertical stratification. The reduction of the stratification occurs because the reduced horizontal salinity gradient reduces the gravitational circulation which acts to decrease the stratification. Monismith et al. (2002), and Geyer and Chant (2006) show that, to leading order, friction balances the baroclinic pressure gradient caused by the longitudinal salinity gradient, from which they demonstrate that the magnitude of the estuarine circulation depends on the horizontal salinity gradient. As shown by the depth-averaged longitudinal salinity profiles in Fig. 15, the stronger vertical stratification resulting from the TVD scheme leads to nonlinear feedback between vertical mixing and stratification. The nonlinear feedback reduces the vertical mixing, which leads to more salinity intrusion for run *A* over run *C*. Fig. 16 depicts the

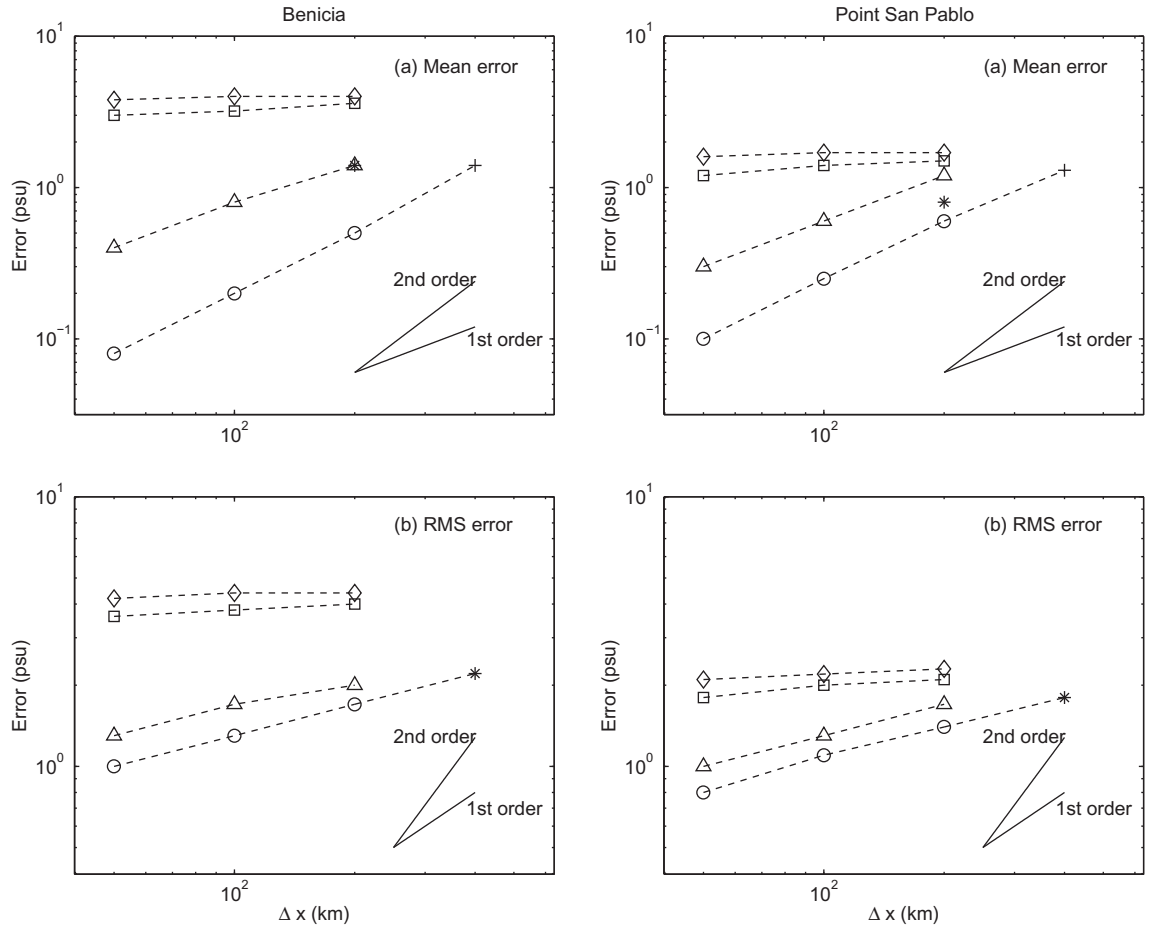

Fig. 13. Convergence of the mean (a) and RMS (b) bottom salinity errors (in psu) as a function of grid refinement Δx at Benicia and Point San Pablo. Legend: Run A (○), Run B (△), Run C (□), Run D (◇), result of Gross et al. (2010) (∗), result of MacWilliams et al. (2007) (+).

Table 6
Least-squares fitted convergence rates for runs *A–D*.

Runs	Benicia		Point San Pablo	
	Mean	RMS	Mean	RMS
A	1.3	0.38	1.4	0.45
B	0.90	0.31	1.0	0.38
C	0.13	0.076	0.16	0.076
D	0.037	0.033	0.043	0.065

vertical eddy-diffusivity over time at Benicia and shows that indeed the vertical eddy-diffusivity is substantially lower when the TVD scheme is employed.

Overlaid on the results in Fig. 13 are the errors computed by MacWilliams et al. (2007), and Gross et al. (2010). MacWilliams et al. (2007) employed the UnTRIM model using an unstructured grid with a nominal resolution of 400 m in the Bay, while Gross et al. (2010) used the Cartesian-grid TRIM model with a fixed horizontal resolution of 200 m. Although those simulations were calibrated over much longer periods than the present simulations, it is still useful to compare their results to ours in the context of understanding the impact of grid resolution. UnTRIM and TRIM employ the same TVD scheme as in SUNTANS (which is based on the method of Casulli and Zanolli (2005)). While the turbulence models are different, the relative impact of different two-equation turbulence models on the salinity predictions is very small (Wang et al., 2011). All three codes employ the same first-order Eulerian–Lagrangian method for momentum advection. Because the implementations are very similar to one another, differences in predictions can be attributed solely to grid resolution. This is clearly demonstrated in Fig. 13. Both the mean and RMS errors computed by MacWilliams et al. (2007) at Benicia and Point San Pablo are on the same asymptotic trajectories as those inferred from the results of run *A*. The mean error of Gross et al. (2010) is slightly higher than the results for run *A* at the same grid resolution. It is difficult to determine the source of the small difference of 1.0 psu at Benicia and 0.5 psu at Point San Pablo between our model and that of Gross et al. (2010), particularly since the result of Gross et al. (2010) was calibrated over a one-year period. Nevertheless, these results suggest that the differences between the results are mainly due to grid resolution and not to the details of the implementation or numerical methods.

5.2. Salt flux analysis

In this section we quantify the effects of grid resolution, the turbulence model and the scalar transport scheme on the salt flux. We compare tidally-averaged steady state salt fluxes at a cross-section in Carquinez Strait (at the location of Benicia in Fig. 1) for Runs *A–D* on the fine and coarse meshes. The salt flux simulations are performed with simplified forcing that employ idealized tides. To ensure periodicity, only two constituents are employed, namely the M2 component and an idealized K1 component which has a period that is exactly double that of M2. Simulations are run over 50 K1 cycles until the tidally-averaged salt flux is roughly in steady

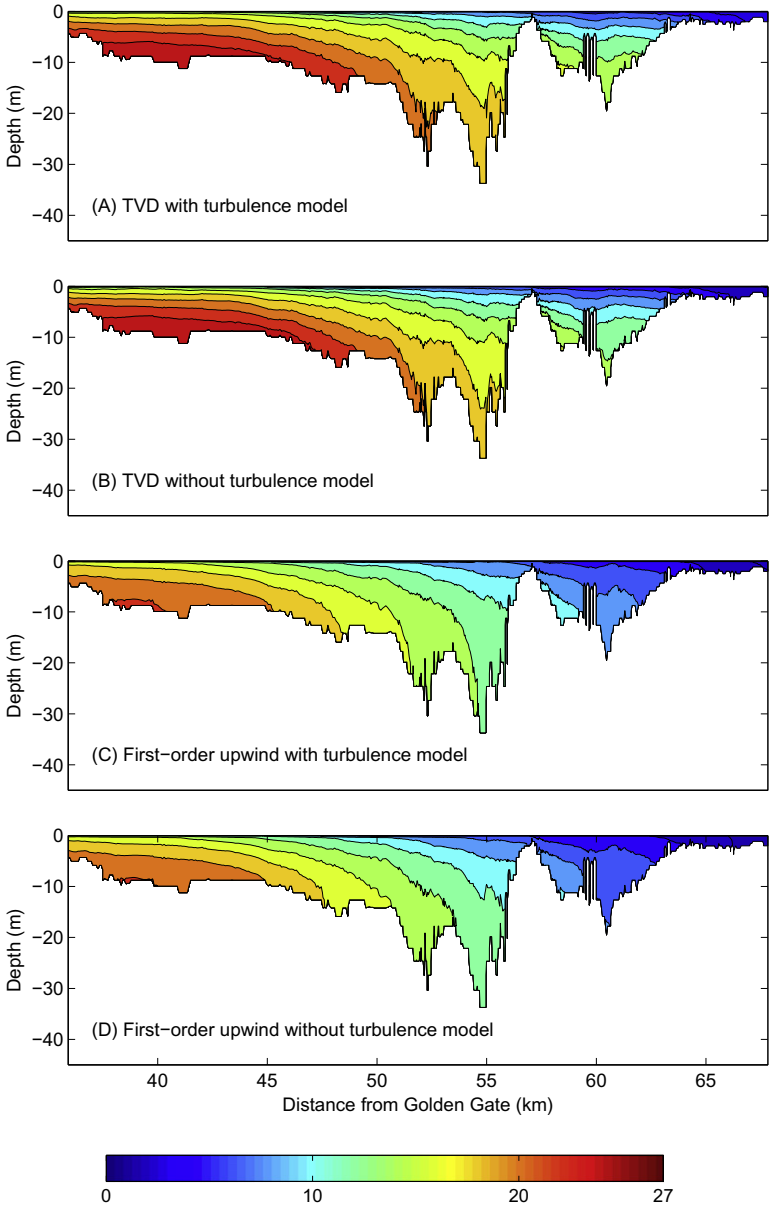

Fig. 14. Vertical profiles of salinity (in psu) along the transect depicted in Fig. 1 in Carquinez Strait tidally-averaged on year day 44 on the finest mesh. Runs: (A) TVD with turbulence model (B) TVD without turbulence model (C) First-order upwind with turbulence model (D) First-order upwind without turbulence model.

state. We assume steady state is reached when the difference between the seaward advection of salt is balanced by landward dispersion by less than 5% (i.e. (advective flux − dispersive flux)/(advective flux)<5%).

Following Fischer et al. (1979), if $\langle\cdot\rangle$ represents the tidal average and $\bar{\cdot}$ represents the cross-sectional integral, then the velocity normal to a cross section, u, and the salinity at the cross section, s, can be decomposed with:

$$u = u_0 + u_1 + u_2,$$
$$s = s_0 + s_1 + s_2,$$

where the tidally-averaged and area-integrated velocity flow rate is $u_0 = <\bar{u}>$ and the tidally-averaged and area-integrated salinity is $s_0 = <\bar{s}>$. The cross-sectionally varying, tidally-averaged terms are:

$$u_1 = \langle u\rangle - u_0,$$
$$s_1 = \langle s\rangle - s_0,$$

and the cross-sectionally varying, tidally-varying terms are:

$$u_2 = \bar{u} - u_0,$$
$$s_2 = \bar{s} - s_0.$$

The tidally-averaged salt flux through a cross-section can then be written as:

$$F = \left\langle \int (u_0 + u_1 + u_2)(s_0 + s_1 + s_2)dA \right\rangle$$
$$= \underbrace{u_0 s_0 A_0}_{F_R} + \underbrace{\int u_1 s_1 \, dA_0}_{F_E} + \underbrace{\left\langle \int u_2 s_2 dA \right\rangle}_{F_T}, \quad (15)$$

where F_R is the river flux, F_E is the steady exchange flux, F_T is the tidal flux, and $A_0 = \overline{A}$ is the tidally-averaged cross-sectional area. The river flux represents mean seaward advection, while the steady exchange and tidal terms account for dispersive mechanisms. These fluxes for Runs *A–D* on the fine and coarse meshes are shown in Fig. 17. The figure also shows $\nu = F_T/(F_E + F_T)$, which represents the ratio of tidal to total dispersive flux (Hansen and Rattray, 1965),

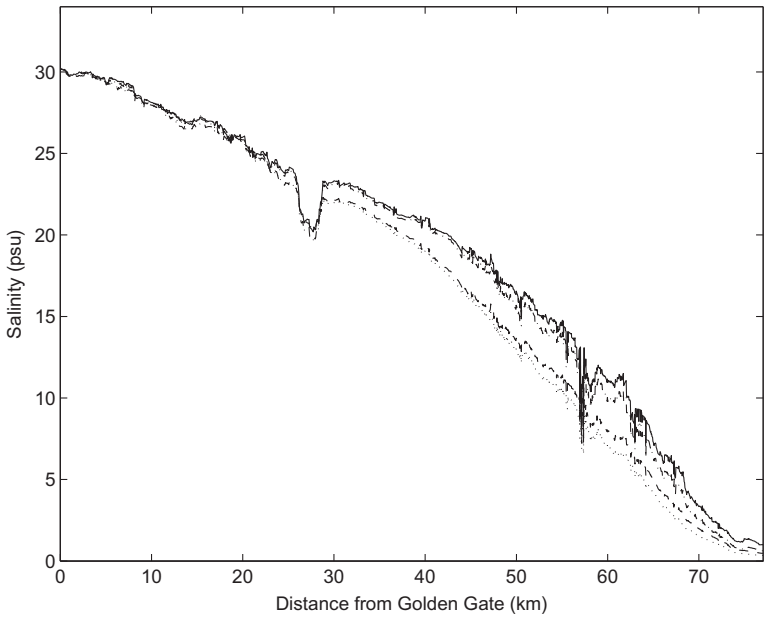

Fig. 15. Depth-averaged salinities (in psu) from the Golden Gate along the longitudinal axis in North San Francisco Bay. Legend: (A) TVD with turbulence model (—), (B) TVD without turbulence model (-··-), (C) First-order upwind with turbulence model (--), (D) First-order upwind without turbulence model (···). Results are computed for the finest mesh.

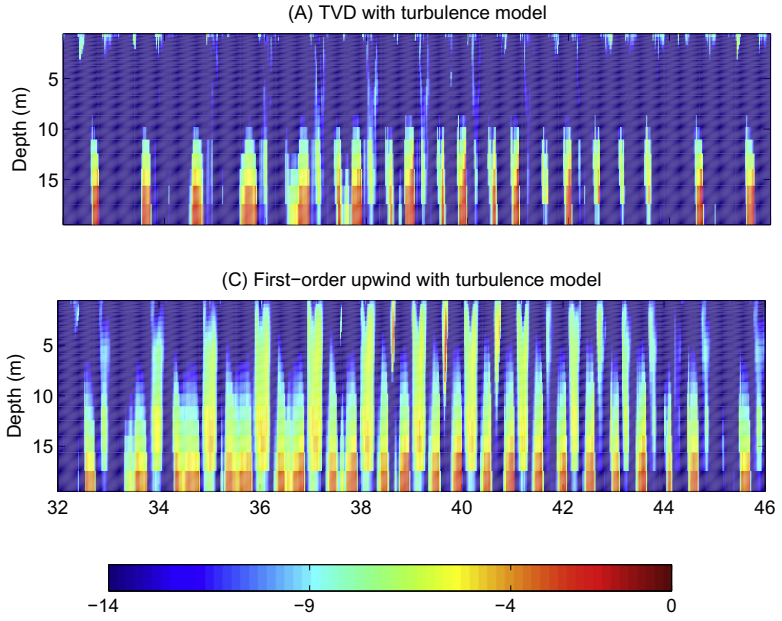

Fig. 16. Time series of vertical profiles of the vertical eddy-diffusivity (in log (m^2s^{-1})) at Benicia on the finest mesh.

and $1 - v = F_E/(F_E + F_T)$, which represents the ratio of steady exchange flux to the total dispersive flux.

Fig. 17 shows that the relative effect of the grid resolution on the salt fluxes is weak when first-order upwinding is used (runs *C* and *D*). For these runs strong numerical diffusion reduces the horizontal salinity gradients, which results in weaker baroclinic circulation and smaller stratification. This is seen in observations by Geyer (2010) in the Hudson River estuary and Monismith et al. (2002) in San Francisco Bay where the strong horizontal salinity gradient induces a baroclinic pressure gradient, which drives estuarine circulation and suppresses vertical mixing to increase stratification. We observe that the steady exchange flux, F_E is smaller than the tidal flux, F_T with first-order upwinding. When the TVD scheme is used, the resulting compressed horizontal salinity gradients lead to exchange fluxes that are larger than the tidal fluxes regardless of whether or not the turbulence model is used. Lack of the turbulence model decreases the exchange flux for runs *A* and *B* on both the fine and coarse meshes. The absence of vertical mixing leads to stronger estuarine circulation, and this weakens the longitudinal salinity gradient. The result is a reduced estuarine circulation and decreased exchange flux. This is described by Park and Kuo (1996) who show the effect of variation in vertical mixing on estuarine circulation over short and long time scales in a numerical model application to Chesapeake Bay. While lack of

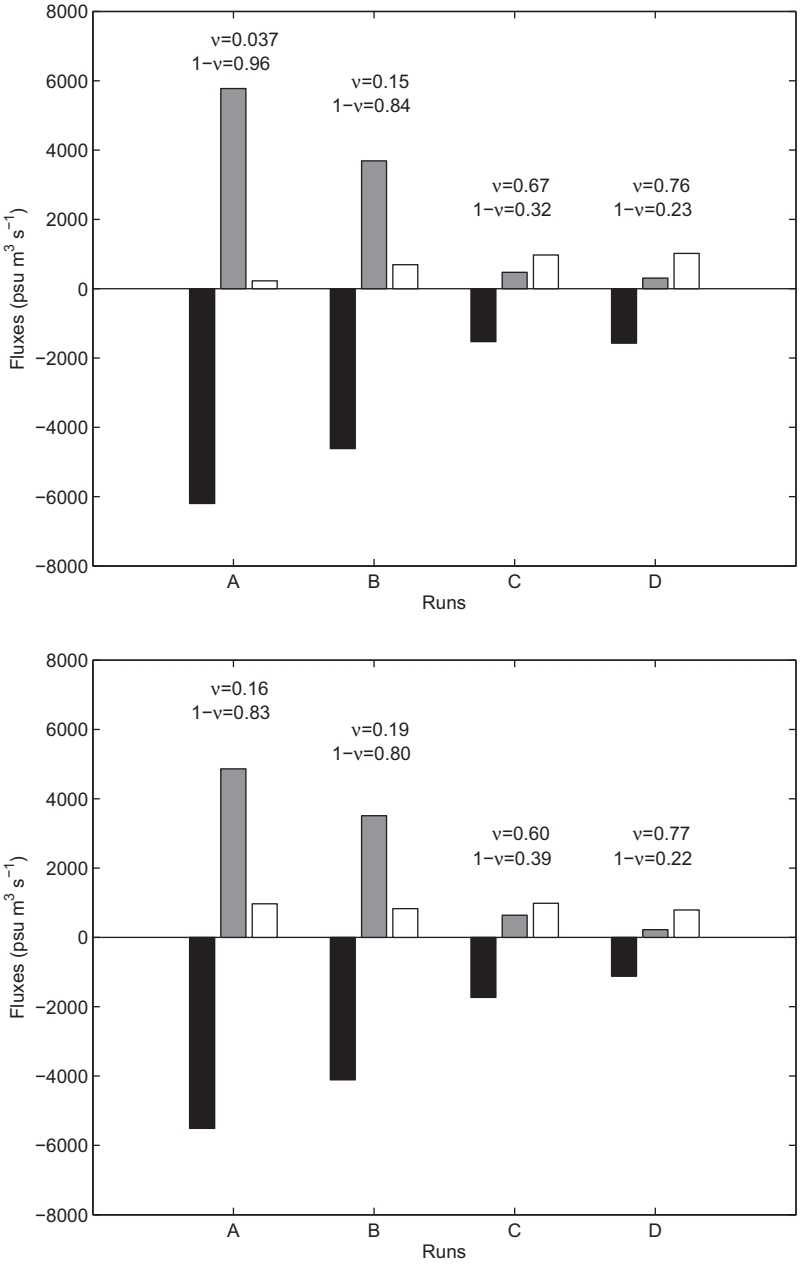

Fig. 17. Influence of the scalar advection scheme and turbulence model on tidally-averaged salt fluxes (in psu m^3 s^{-1}) on fine (top) and coarse (bottom) meshes. Runs: (A) TVD with turbulence model, (B) TVD without turbulence model, (C) First-order upwind with turbulence model, (D) First-order upwind without turbulence model. Legend: Black: F_R, Gray: F_E, White: F_T. Diffusive fraction $\nu = F_T/(F_T + F_E)$ and $1 - \nu = F_E/(F_T + F_E)$.

vertical mixing produces stronger estuarine circulation, lack of the turbulence model on the fine mesh significantly increases the tidal flux (ν increases by a factor of four). On the coarse mesh, lack of the turbulence model for run *B* has very little effect on the tidal flux but instead leads to a river flux that is smaller roughly by an amount equal to the decrease in steady exchange flux. Therefore, the value of ν remains relatively unchanged on the coarse mesh for runs *A* and *B*.

6. Conclusions

In this paper, we describe three-dimensional simulations of San Francisco Bay performed with the unstructured-grid SUNTANS model. A TVD scalar transport scheme is included in the model and modified to work for flows with extensive wetting and drying. The model inputs include high resolution bathymetry from the NGDC database and an unstructured grid that enables refinement of the complex coastline. The model is tidally forced with water surface elevations at the open ocean boundary. Freshwater inflow estimates from the DAYFLOW program are imposed as flow boundary conditions at the Delta boundary. A 45-day three-dimensional simulation runs roughly ten times faster than real time. The bottom roughness is adjusted to reproduce the observed sea-surface heights and currents with the model. With no further tuning, the model is validated with salinity observations in North San Francisco Bay.

The model-predicted surface elevations and depth-averaged currents compare well with observations. The tidal hydrodynamics are reproduced by the model, thus validating the inputs and

parameterizations employed. The spring and neap tidal cycles, and the mixed semi-diurnal and diurnal tidal ranges for surface elevations and depth-averaged currents are reproduced by the model at all stations. The hydrodynamic calibrations demonstrate that the model predicts tidal propagation through Golden Gate and the spatial distribution of surface elevations and depth-averaged currents in San Francisco Bay well. Comparisons of predicted velocity profiles with observations do not match as well due to the effects of bathymetry which makes the bottom boundary layers difficult to model. The model realistically predicts the tidal time scale variability in salinity. The salinity predictions also capture the periodic stratification of the estuary by obtaining with a high degree of accuracy the surface and bottom salinity at PSP and BEN. This indicates the MY2.5 turbulence closure scheme represents the effects of stratification on turbulence reasonably well for North San Francisco Bay.

A grid resolution study indicates that model convergence is highly sensitive to the choice of the advection scheme and the turbulence model. The best convergence rate in space is achieved when the TVD scheme is employed for salt transport and the turbulence model is employed. This accuracy degrades without the turbulence model due to the lack of feedback between vertical mixing and stratification. The result is an increase in error by one order of magnitude and a smaller convergence rate. Use of first-order upwinding further increases the errors roughly by a factor of two. Despite an expected first-order rate of convergence, these errors do not decrease when the mesh is refined. The impact of the turbulence model on the errors is also negligible when first-order upwinding is used.

Lack of convergence and large errors when first-order upwinding is used result from horizontal numerical diffusion that leads to a diffuse salt wedge and decreased baroclinic circulation. The errors are much more sensitive to mesh refinement and the turbulence model when the TVD scheme is used because of the increased horizontal salinity gradient. This ensures that nonlinear feedback between vertical mixing and stratification can take place when the turbulence model is employed. A diffuse salt wedge prevents the formation of sufficient vertical stratification that would damp the vertical mixing and lead to further salinity intrusion.

A salt-flux analysis shows that, when first-order upwinding is used, the salt flux does not change when the grid is refined or when the turbulence model is employed. Horizontal salinity gradients are so weak that the tidal flux of salt is larger than the steady exchange flux. This is in contrast to the results of using the TVD scheme, which shows that the salt fluxes are smaller on the coarse mesh than on the fine mesh. Use of the TVD scheme produces a compressed salinity front that resolves more of the baroclinic circulation. This has the effect of producing a larger tidal flux to balance the river flux without the turbulence model. On the coarse mesh, lack of the turbulence model does not change the tidal flux, but instead the reduction of the river flux is balanced by an equal reduction in the exchange flux.

Acknowledgments

Chua acknowledges the support of the Singapore National Research Foundation (Environment and Water Technologies) Ph.D. Scholarship. Chua and Fringer acknowledge the support of ONR grant N00014-08-1-0904 (Scientific officers: Dr. C. Linwood Vincent, Dr. Terri Paluszkiewicz, and Dr. Scott Harper). We also acknowledge the support of the California State Coastal Conservancy (Agreement Number 07-137; Program managers Abe Doherty, Doug George, and Matt Gerhart). Simulations were conducted on the Peter A. McCuen Environmental Computing Center at Stanford University.

References

Casulli, V., 1990. Semi-implicit finite difference methods for the two-dimensional shallow water equations. J. Comput. Phys. 86, 56–74.
Casulli, V., Cattani, E., 1994. Stability, accuracy and efficiency of a semi-implicit method for three-dimensional shallow water flow. Comput. Math. Appl. 27, 99–112.
Casulli, V., Walters, R.A., 2000. An unstructured grid, three-dimensional model based on the shallow water equations. Int. J. Numer. Methods Fluids 32, 331–348.
Casulli, V., Zanolli, P., 2005. High resolution methods for multidimensional advection–diffusion problems in free-surface hydrodynamics. Ocean Modell. 10, 137–151.
CDWR, 1986. DAYFLOW program documentation and data summary user's guide. Technical report. California Department of Water Resources, Sacramento, CA.
Cheng, R.T., Casulli, V., Gartner, J.W., 1993. Tidal, residual, intertidal mudflat (TRIM) model and its applications to San Francisco Bay, California. Estuar. Coast. Shelf Sci. 36, 235–280.
Cheng, R.T., Ling, C.H., Gartner, J.W., Wang, P.F., 1999. Estimates of bottom roughness length and bottom shear stress in South San Francisco Bay, California. J. Geophys. Res. 104, 7715–7728.
Cheng, R.T., Smith, R.E., 1998. A Nowcast model for tides and tidal currents in San Francisco Bay, California. In: Proceedings, Ocean Community Conference. Marine Technology Science, Baltimore, MD, pp. 537–543.
Cloern, J.E., Nichols, F.H., 1985. Time scales and mechanisms of estuarine variability, a synthesis from studies of San Francisco Bay. Hydrobiol 129, 229–237.
Conomos, T.J., 1979. Properties and circulation of San Francisco Bay waters. In: Conomos, T.J. (Ed.), San Francisco Bay: The Urbanized Estuary. AAAS, Pacific Division, San Francisco, CA, pp. 47–84.
Conomos, T.J., Smith, R.E., Gartner, J.W., 1985. Environmental setting of San Francisco Bay. Hydrobiol 129, 1–12.
Darwish, M.S., Moukalled, F., 2003. TVD schemes for unstructured grids. Int. J. Heat Mass Transfer 46, 599–611.
Dever, E.P., Lentz, S.J., 1994. Heat and salt balances over the northern California shelf in winter and spring. J. Geophys. Res. 99, 16001–16017.
Fischer, H.B., List, E.J., Koh, R.C.Y., Imberger, J., Brooks, N.H., 1979. Mixing in Inland and Coastal Waters. Academic Press, San Diego, CA.
Fringer, O.B., Gerritsen, M., Street, R.L., 2006. An unstructured-grid, finite-volume, nonhydrostatic, parallel coastal ocean simulator. Ocean Modell. 14, 139–173.
Fringer, O.B., Street, R.L., 2005. Reducing numerical diffusion in interfacial gravity wave simulations. Int. J. Numer. Methods Fluids 49, 301–329.
Galperin, B., Kantha, L.H., Hassid, S., Rosati, A., 1988. A quasi-equilibrium turbulent energy model for geophysical flows. J. Atmos. Sci 45, 55–62.
Geyer, W.R., 2010. Estuarine salinity structure and circulation. In: Valle-Levinson, A. (Ed.), Contemporary Issues in Estuarine Physics. Cambridge University Press, pp. 12–26.
Geyer, W.R., Chant, R., 2006. Physical oceanography processes in the Hudson River estuary. In: Levinton, J.S., Waldman, J.R. (Eds.), The Hudson River Estuary. Cambridge University Press.
Gross, E.S., Koseff, J.R., Monismith, S.G., 1999a. Evaluation of advective schemes for estuarine salinity simulations. J. Hydraul. Eng. 125, 32–46.
Gross, E.S., Koseff, J.R., Monismith, S.G., 1999b. Three-dimensional salinity simulations of South San Francisco Bay. J. Hydraul. Eng. 125, 1199–1209.
Gross, E.S., Bonaventura, L., Rosatti, G., 2002. Consistency with continuity in conservative advection schemes for free-surface models. Int. J. Numer. Methods Fluids 38, 307–327.
Gross, E.S., MacWilliams, M.L., Kimmerer, W., 2005. Simulating periodic stratification in the San Francisco Estuary. In: Proceedings of the 9th International Conference on Estuarine and Coastal Modeling, ASCE Conference Proceedings. pp. 155–175.
Gross, E.S., MacWilliams, M.L., Kimmerer, W.J., 2010. Three-dimensional modeling of tidal hydrodynamics in the San Francisco Estuary. San Francisco Estuary Watershed Sci. 7, 1–37.
Hansen, D.V., Rattray, M., 1965. Gravitational circulation in straits and estuaries. J. Mar. Res. 23, 104–122.
Harten, A., 1983. High resolution schemes for hyperbolic conservation laws. J. Comput. Phys. 49, 357–393.
Ip, J.T.C., Lynch, D.R., Friedrichs, C.T., 1998. Simulation of estuarine flooding and dewatering with application to Great Bay, New Hampshire. Estuar. Coast. Shelf Sci. 47, 119–141.
Kimmerer, W.J., 2002. Physical, biological and management responses to variable freshwater inflow into the San Francisco Estuary. Estuaries 25, 1275–1290.
Largier, J.L., 1996. Hydrodynamic exchange between San Francisco Bay and the ocean: the role of ocean circulation and stratification. In: Hollibaugh, J.T. (Ed.), San Francisco Bay: The Ecosystem. AAAS, San Francisco, CA, pp. 69–104.
MacWilliams, M.L., Cheng, R.T., 2006. Three-dimensional hydrodynamic modeling of San Pablo Bay on an unstructured grid. In: Proceedings of the 7th International Conference on Hydroscience Engineering, Philadelphia, USA.
MacWilliams, M.L., Gross, E.S., DeGeorge, J.F., Rachiele, R.R., 2007. Three-dimensional hydrodynamic modeling of the San Francisco Estuary on an unstructured grid. In: Proceedings of International Association of Hydraulic Engineering and Research, Venice, Italy.
Mellor, G.L., Yamada, T., 1982. Development of a turbulence closure model for geophysical fluid problem. Rev. Geophys. Space Phys. 20, 851–875.

Monismith, S.G., Kimmerer, W., Burau, J.R., Stacey, M.T., 2002. Structure and flow-induced variability of the subtidal salinity field in northern San Francisco Bay. J. Phys. Oceanogr. 32, 3003–3019.

Nepf, H.M., 1999. Drag, turbulence, and diffusion in flow through emergent vegetation. Water Resour. Res. 35, 479–489.

Oltmann, R.N., 1998. Indirect measurement of delta outflow using ultrasonic velocity meters and comparison to mass-balance calculated outflow. IEP Newsletter 11, 5–8.

Park, K., Kuo, A.Y., 1996. Effect of variation in vertical mixing on residual circulation in narrow, weakly nonlinear estuaries. In: Aubrey, D.G., Friedrichs, C.T. (Eds.), Buoyancy Effects on Coastal and Estuarine Dynamics. American Geophysical Union, pp. 301–317.

Roe, P.L., 1984. Generalized formulation of TVD Lax–Wendroff schemes. NASA Langley Research Center Technical Report. ICASE Report 84-53. NASA CR-172478.

Sankaranarayanan, S., McCay, D.F., 2003. Application of a two-dimensional depth-averaged hydrodynamic tidal model. Ocean Eng. 30, 1807–1830.

Sweby, P.K., 1984. High resolution schemes using flux limiters for hyperbolic conservation laws. SIAM J. Numer. Anal. 21, 995–1011.

Walters, R.A., Cheng, R.T., Conomos, T.J., 1985. Time scales of circulation and mixing processes of San Francisco Bay waters. Hydrobiologia 129, 13–36.

Wang, B., Fringer, O.B., Gridding, S.N., Fong, D.A., 2008. High-resolution simulations of a macrotidal estuary using SUNTANS. Ocean Modell. 28, 167–192.

Wang, B., Giddings, S.N., Fringer, O.B., Gross, E.S., Fong, D.A., Monismith, S.G., 2011. Modeling and understanding turbulent mixing in a macrotidal salt wedge estuary. J. Geophys. Res. 116, C02036. doi:10.1029/2010JC006135.

Zheng, L.C., Liu, C.H., 2003. A modeling study of the Satilla River Estuary, Georgia Part I: flooding-drying process and water exchange over the salt marsh-estuary-shelf complex. Estuaries 26, 651–669.